Heliyon 9 (2023) e17725

Contents lists available at ScienceDirect

Heliyon

journal homepage: www.cell.com/heliyon

Research article

Gamma-ray, fast neutron and ion shielding characteristics of low-density and high-entropy Mg–Al–Ti–V–Cr–Fe–Zr–Nb alloy systems using Phy-X/PSD and SRIM programs

Basanta Subedi, Jeevan Paudel, Tika Ram Lamichhane *

Central Department of Physics, Tribhuvan University, Kirtipur, Kathmandu, 44600, Nepal

ARTICLE INFO

Keywords:
High-entropy alloys (HEAs)
Absorption coefficients
Build-up factors (BUFs)
Removal cross-section (Σ_R)
Stopping power (TSP)
Phy-X/PSD
SRIM

ABSTRACT

This study aimed to assess the radiation shielding properties of ten low-density high-entropy alloys (LWHEAs) using Phy-X/PSD software to analyze various shielding parameters, such as attenuation coefficients (μ_m and μ), mean free path (λ), effective atomic number (Z_{eff}), and removal cross-section (Σ_R), in the energy range of 15 keV to 15 MeV. A comprehensive evaluation was performed to compare the attenuation outcomes provided by HEAs with a range of shielding materials documented in the literature. The study also calculated the build-up factors (BUFs) of the alloys by using the GP-fitting interpolation method. The stopping power of the alloys against H^1/He^{+2} ions was analyzed using the SRIM Monte Carlo code, considering total stopping power (TSP) and projected range (PR). The results indicated that HEA8 ($Al_{3.88}Cr_{14.95}Mo_{27.58}Nb_{26.71}Ti_{13.76}Zr_{13.11}$) had the best performance in terms of shielding against γ-rays, fast neutrons, and H^1/He^{+2} ions, as it achieved the highest values of parameters such as μ_m, μ, Z_{eff}, and Σ_R, along with the lowest values of HVL, TVL, λ, BUFs (0.1–5 MeV), TSP, and PR. On the other hand, HEA10 ($Mg_{10.77}Al_{11.96}Mn_{24.35}Fe_{24.75}Cu_{28.17}$) had the lowest BUFs in both lower (0.015–0.08 MeV) and higher (5–15 MeV) energy regions. The order of μ_m for the alloys was found to be HEA5 < HEA6 < HEA9 < HEA7 < HEA10 < HEA4 < HEA2 < HEA3 < HEA1 < HEA8. The study concluded that LWHEAs possess superior radiation shielding properties compared to conventional materials, making them a promising new class of materials for radiation shielding applications.

1. Introduction

The exponential rise in the utilization of radioactive sources across diverse fields, including medicine, agriculture, industries, space exploration, and power generation, coupled with advancements in technology and communication, has led to increased human exposure to various forms of ionizing radiation, which may impose a deleterious impact on the biological system if exposed for an extended period [1–5]. Climate change's reality has compelled the utilization of nuclear power plants, serving as distinct energy sources; nevertheless, these plants emit multiple hazardous radiations, including X-rays and γ-rays. Despite the concerns that the nuclear catastrophes at Three Mile Island, Chernobyl, and Fukushima Daiichi raised about these facilities, throughout the past 60 years, significant advancements in nuclear power generation using nuclear power plants have been recognized [6]. Utilizing

* Corresponding author.
E-mail address: tika.lamichhane@cdp.tu.edu.np (T.R. Lamichhane).

https://doi.org/10.1016/j.heliyon.2023.e17725
Received 7 March 2023; Received in revised form 25 June 2023; Accepted 26 June 2023

Available online 30 June 2023

Table 1
The chemical compositions (by %wt) and densities of ten different HEA samples.

Sample	Chemical compositions (%wt)																Density (ρ)
code	Li	Be	Mg	Al	Si	Sc	Ti	V	Cr	Mn	Fe	Ni	Cu	Zr	Nb	Mo	g/cm^3
HEA1	–	–	–	–	–	–	16.33	16.32	–	–	–	–	–	30.74	36.61	–	6.52
HEA2	–	–	–	–	–	–	13.61	27.78	–	–	–	–	–	27.82	30.78	–	6.34
HEA3	–	–	–	–	–	–	15.96	–	17.85	–	–	–	–	31.57	34.62	–	6.67
HEA4	–	–	–	–	–	–	14.19	14.88	15.65	–	–	–	–	27.59	27.69	–	6.57
HEA5	4.26	–	7.46	16.57	–	27.61	44.09	–	–	–	–	–	–	–	–	–	2.67
HEA6	–	5.34	–	15.99	12.48	–	49.64	–	–	–	16.55	–	–	–	–	–	3.91
HEA7	–	–	11.37	12.63	–	–	22.40	–	–	–	26.13	27.47	–	–	–	–	4.64
HEA8	–	–	–	3.88	–	–	13.76	–	14.95	–	–	–	–	13.11	26.71	27.58	6.93
HEA9	–	–	3.64	23.59	–	–	41.85	12.73	18.19	–	–	–	–	–	–	–	4.05
HEA10	–	–	10.77	11.96	–	–	–	–	–	24.35	24.75	–	28.17	–	–	–	4.946

radiation-resistant materials, such as those effective against X-rays and γ-rays, is essential. It is therefore imperative to employ suitable shielding materials not only to mitigate the adverse biological impacts of radiation but also to ensure effective management of radiation waste. In this context, scientists and engineers in the field of materials continuously seek low-density structural materials to minimize energy consumption, operational expenses, and radiation-related risks [7,8]. Those materials with properties like high density, high melting temperature, high mechanical strength, high corrosion resistance, and cheap cost, are of particular importance in radiation shielding fields. Lead (Pb), despite being a commonly used element for radiation protection due to its high density and atomic number (Z), has limitations such as high toxicity, weak mechanical strength, and a low melting point. These factors render it inadequate for radiation protection applications on its own [9,10]. Furthermore, Pb shields exhibit limited absorption capability within the 40 to 88 keV energy range, referred to as the lead feeble absorption region [11]. A plethora of research including those on various ceramics [12–15], polymer composites [16–18], glass systems [19–21], and metal alloys [22–26] has been conducted in a search of efficient materials that could replace conventional shielding facilities offered by Pb-based materials and different types of concretes. In our previous work [27], we investigated and compared the radiation shielding properties of lightweight Ti-based bulk metallic glasses with traditional Pb and heavy concrete materials.

In the light of the above-mentioned limitations associated with conventional shielding agents, a new class of structural and functional materials called high entropy alloys (HEAs), which are prepared primarily by mixing at least five primary elements in equal or near equimolar concentration between 5 and 35%, and exhibit some exceptional characteristics such as high strength and thermal stability, good fatigue, high fracture and corrosion resistance, and oxidation resistance, may address these caveats [28–31]. Such alloys are so-called because they exhibit much higher mixing entropy that makes them superior over traditional alloys, which have often been based on one or two main components over thousands of years because of the expected formation of several complicated inter-metallic compounds making them brittle and challenging to handle and analyze [28,31]. The adverse impact on alloy properties caused by the formation of undesired phases or intermetallic compounds is mitigated by the high configuration entropy inherent in HEAs, resulting in the formation of a solid solution comprising either a face-centered cubic (FCC) or a body-centered cubic (BCC) structure, or a combination of these phases [31,32]. Some of the many applications of such next-generation materials include fields such as biomedical devices, chemical plants, submarines, aircraft, and golf club heads [33–35]. Many physical, mechanical, structural, and hardness assessments of many HEAs, which are formed mostly from elements like Cr, Fe, Co, and Ni, have been elucidated previously by many researchers. For example, compression, microstructure, and deformation characteristics at different temperatures of four different Ti-based HEAs were studied previously by Senkov et al. [34]. Many other HEAs such as $Al_{20}Li_{20}Mg_{10}Sc_{20}Ti_{30}$ (by Youssef et al. [36]), $Al_{20}Be_{20}Fe_{10}Si_{15}Ti_{35}$ (by Tseng et al. [28]), $Al_{20}Fe_{20}Mg_{20}Ni_{20}Ti_{20}$ (by Mishra et al. [37]), $Al_{10}Cr_{20}Mo_{20}Nb_{20}Ti_{20}Zr_{10}$ (by Waseem et al. [38]), $Al_{35}Cr_{14}Mg_{6}Ti_{35}V_{10}$ (by Chauhan et al. [39]), and MgAlMnFeCu (by Pandey et al. [40]) were synthesized and characterized through XRD, TEM, and SEM analyses. Even though, to the best of our knowledge, there haven't been many studies conducted, a rigorous review of the literature has led us to the conclusion that HEAs might become the radiation shielding materials of the future. Recent research by Gul et al. explored the nuclear radiation attenuation capacity of the newly synthesized NiCoFeCrW HEA composite, revealing significant improvements in hardness, compression strength, and neutron shielding capacity [31]. Some other researchers have also conducted studies on various HEAs, revealing their potential as a new class of materials for radiation protection [32,41,42]. In these regards, this study was proposed to assess the radiation, fast neutrons, and different charged particles like H^1/He^{+2} ions shielding abilities of several low-density HEAs. The radiation shielding results obtained for these alloys have been compared to those of available HEAs as well as several other standard shielding materials such as glass composites, concretes, lead-based, and lead-free glasses.

2. Materials and methods

In this work, ten different low-density HEAs were considered for their radiation shielding assessment. The elemental compositions (in %wt fraction) and experimentally measured densities of considered HEAs were adopted from the literature [28,34,36–40] and are presented in Table 1. The detailed synthesis procedure as well as several other structural, physical, and mechanical characteristics of these HEAs were described in this literature. So, this study primarily focuses on their γ-ray, fast neutrons, and H^1/He^{+2} ions shielding ability assessment.

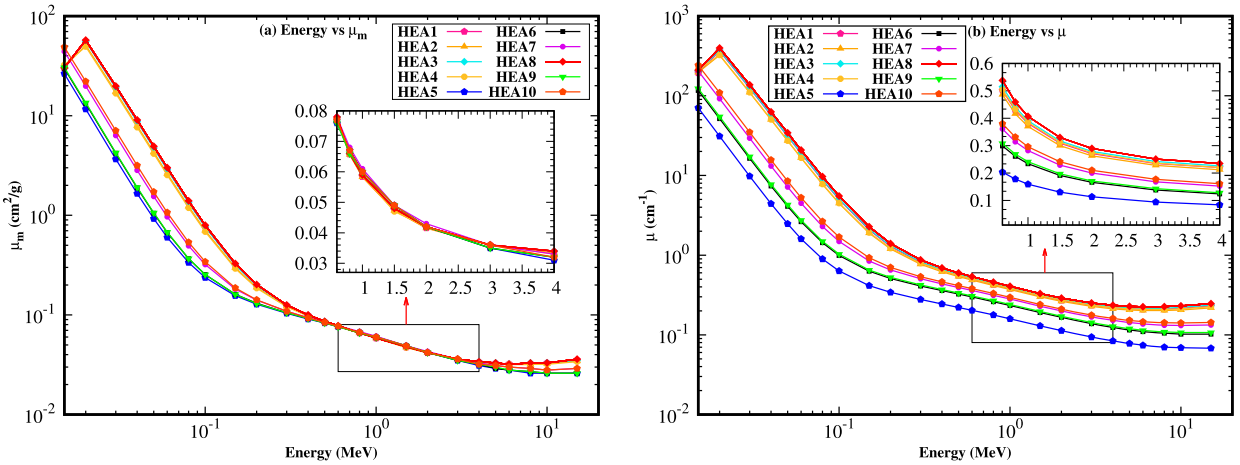

Fig. 1. Behaviors of (a) μ_m, and (b) μ as a function of energy of the radiation.

The nuclear radiation shielding assessment of the proposed alloys was performed using the user-friendly online Phy-X/PSD software developed by Sakar et al. [43]. Any user can calculate different shielding properties of metal, alloys, compounds, and composites using Phy-X/PSD software after registering on the website available at: https://phy-x.net/PSD, through the email address verification. The server an Intel (R) Core(TM) i7-2600 CPU @ 3.40 GHz CPU with 1 GB-installed memory and operating on Ubuntu 14.04.3 LTS system can calculate shielding properties in two different energy ranges: one from 0.015–15 MeV and another from 1 keV–100 GeV. The different shielding properties that this software can calculate are linear attenuation coefficient (μ), mass attenuation coefficient (μ_m), half value layer (HVL), tenth value layer (TVL), mean free path (λ), effective atomic number (Z_{eff}), exposure and energy absorption build-up factors (EBF and EABF), fast neutron removal cross-section (Σ_R), effective conductivity (C_{eff}), and effective electron density (N_{eff}). Furthermore, the stopping ability of HEAs against H^1/He^{+2} ions were determined using the SRIM Monte Carlo program. SRIM (Stopping and Range of Ions in Matter) is a widely used computer program for simulating the interactions of ions with matter, providing valuable insights into ion implantation, radiation damage, and material characterization [44]. The detailed theoretical background for each shielding parameter can be found elsewhere in the literature [6,32,45].

3. Results and discussion

The μ (cm^{-1}) is a constant that describes the fraction of incident photons in a mono-energetic beam per unit thickness of a material. It can be evaluated using popular Beer-Lambert's law in the form: $\mu = \frac{1}{x} ln(\frac{I_0}{I})$, where I_0 and I are the original intensity and intensity at a depth of x cm. Similarly, μ_m (cm^2/g) is the normalization of μ per unit density of material (i.e., $\mu_m = \frac{\mu}{\rho}$) [43,46]. The γ-ray shielding parameters for selected HEAs were determined for a wide energy range of 0.015–15 MeV using Phy-X/PSD software. For comparison purposes, such parameters were also evaluated for various energies of γ-ray emitted in radioactive decay of different sources like Am^{241}, Ba^{133}, Cd^{109}, Co^{60}, Cs^{137}, I^{131}, and Na^{22}. Table 2 lists out the μ_m values of studied HEAs that are illustrated in Fig. 1(a) as a function of the energy of radiation. As presented in Fig. 1(a), the maximum values of μ_m can be observed for all HEAs at minimum photon energy, which however decreased exponentially with an increase in energy of the radiation. At the intermediate energy region, the μ_m values for all HEAs decreased steadily. However, μ_m values increased slightly after about 5 MeV. Such behavior of μ_m can be explained based on the dominance effect of different photon-matter interaction phenomena. The maximum values of μ_m for all HEAs at lower energies are due to the predominance of the photoelectric (PE) process (dominant up to 0.1 MeV) whose absorption cross-section is strongly dependent on the atomic number (Z-number) of the material as Z^{4-5} and energy as $1/E^{3.5}$ [46]. The directly proportional relationship of Compton scattering (CS) (dominant at the intermediate range of energy up to 3 MeV) cross-section with Z-number is the reason behind the steady decrement of μ_m values in the intermediate range of energy [47]. However, above 3 MeV, the pair production (PP) is dominant with its cross-section varying as Z^2 (and $log(E)$), which is why μ_m seemed to be increasing slightly. It can be observed from Fig. 1(a) that the sample HEA8 has the highest μ_m values at most of the energies while HEA1 & HEA3 have near equivalent values with HEA8, which may be because of their nearly equal densities and chemical compositions. Similarly, the alloys HEA5, HEA6, and HEA9 have the lowest and almost equal μ_m values. Table 3 presents the comparison of μ_m values of HEA5 and HEA8 with those HEAs reported in the existing literature. The HEA8 alloy exhibits much higher μ_m values compared to three different CoNiFeCr-Ti/Al HEAs and other commonly used shielding materials, including ordinary concrete (OC), steel-scrap (SS), and steel-magnetite (SM), as reported by Sakar et al. [32], across various gamma-ray energy sources. For instance, Sakar et al. reported the highest μ_m value of 12.339 cm^2/g for the $Co_{26.2}Ni_{25.8}Fe_{24.9}Cr_{23.1}$ alloy (referred to as HEA1*) at an energy of 0.0263 MeV. At the same energy, HEA8 exhibited a μ_m value of 29.238 cm^2/g, while HEA5 had a value of 5.311 cm^2/g. In comparison, OC, SS, and SM had values of 1.463, 7.856, and 9.345 cm^2/g, respectively. However, the obtained μ_m values for HEAs under irradiation with photons from a Ba^{133} source are slightly lower compared to the experimental values reported for NiCoFeCrW HEA (represented as HEA*) and NiCoFeCrW-2.5%B_4C composite (represented as HEA Comp.) by Gul

Table 2
Mass attenuation coefficients of studied HEAs at different incident radiation energies.

Energy	Mass attenuation coefficient (μ_m, cm^2/g)									
(MeV)	HEA1	HEA2	HEA3	HEA4	HEA5	HEA6	HEA7	HEA8	HEA9	HEA10
0.015	29.707	31.022	30.909	32.362	26.461	29.832	44.131	30.317	30.505	48.865
0.02	55.949	50.936	55.705	49.385	11.664	13.238	19.856	57.388	13.503	22.071
0.03	19.118	17.341	19.014	16.777	3.673	4.190	6.340	19.819	4.259	7.072
0.04	8.745	7.922	8.693	7.658	1.657	1.886	2.835	9.084	1.912	3.160
0.05	4.748	4.302	4.719	4.158	0.927	1.048	1.547	4.939	1.060	1.717
0.06	2.890	2.621	2.872	2.535	0.601	0.672	0.966	3.007	0.678	1.066
0.08	1.345	1.226	1.337	1.187	0.336	0.367	0.495	1.399	0.369	0.537
0.1	0.768	0.705	0.764	0.684	0.237	0.254	0.321	0.797	0.254	0.342
0.15	0.318	0.298	0.317	0.292	0.156	0.161	0.182	0.328	0.161	0.187
0.2	0.198	0.189	0.197	0.186	0.128	0.131	0.141	0.202	0.130	0.142
0.3	0.124	0.121	0.124	0.121	0.104	0.105	0.109	0.126	0.105	0.109
0.4	0.099	0.098	0.099	0.098	0.091	0.092	0.094	0.100	0.092	0.093
0.5	0.086	0.085	0.086	0.085	0.083	0.083	0.085	0.086	0.083	0.084
0.6	0.077	0.077	0.077	0.077	0.076	0.077	0.078	0.078	0.076	0.077
0.8	0.066	0.066	0.066	0.066	0.067	0.067	0.068	0.066	0.066	0.067
1	0.058	0.058	0.059	0.059	0.060	0.060	0.061	0.059	0.060	0.060
1.5	0.047	0.047	0.048	0.047	0.049	0.049	0.049	0.048	0.049	0.049
2	0.042	0.042	0.042	0.042	0.042	0.042	0.043	0.042	0.042	0.042
3	0.036	0.036	0.036	0.036	0.035	0.035	0.036	0.036	0.035	0.036
4	0.034	0.033	0.034	0.033	0.031	0.032	0.033	0.034	0.032	0.032
5	0.033	0.032	0.033	0.032	0.029	0.029	0.031	0.033	0.030	0.031
6	0.032	0.032	0.032	0.032	0.028	0.028	0.030	0.032	0.028	0.030
8	0.032	0.032	0.033	0.032	0.026	0.027	0.029	0.033	0.027	0.029
10	0.033	0.032	0.033	0.032	0.026	0.026	0.028	0.033	0.026	0.028
15	0.035	0.034	0.035	0.034	0.026	0.026	0.029	0.036	0.026	0.029

Table 3
Comparison of μ_m (cm^2/g) values of HEA5 (least effective) and HEA8 (most effective) with those HEAs and other commonly used shielding materials reported in the literature.

Energy	Present HEAs		Reported by Sakar et al. [32]				Reported by Gul et al. (Expt.) [31]	
(keV)	HEA5	HEA8	HEA1*	OC	SS	SM	HEA*	HEA Comp.
26.3	5.311	29.238	12.339	1.463	7.856	9.345	N/A	N/A
53	0.797	4.177	1.733	0.326	1.149	1.341	N/A	N/A
81	0.329	1.354	0.601	0.202	0.435	0.489	3.813	3.698
160	0.148	0.289	0.184	0.139	0.165	0.171	0.698	0.69
223	0.121	0.174	0.135	0.122	0.129	0.131	0.351	0.34
276	0.108	0.136	0.116	0.112	0.115	0.115	0.239	0.232
302	0.104	0.125	0.110	0.108	0.109	0.109	0.214	0.206
356	0.096	0.109	0.100	0.101	0.101	0.101	0.161	0.16
383	0.093	0.103	0.096	0.098	0.097	0.097	0.144	0.14

* Note: N/A indicates not available.

et al. [31] at seven different photon energies (see Table 3). Furthermore, noticeable discontinuities in the μ_m values or absorption spectrum were observed specifically for HEA1 to HEA4 and HEA8 at an energy of 20 keV. These abrupt changes are attributed to the K X-ray absorption edge of Nb, which occurs at 18.98 keV. In contrast, such pronounced peaks are not observed in other samples, as the absorption edges of the remaining elements are significantly smaller and do not fall within the energy range of 15 keV to 15 MeV. Moreover, almost equal μ_m values in the 0.5–3 MeV energy range can be observed for all selected HEAs from the zoomed portion of Fig. 1(a).

The linear attenuation coefficient (μ) also followed a similar trend to that of μ_m, which can be observed in Fig. 1(b). The only difference between μ_m and μ is that μ is density-dependent but not μ_m. Thus, μ is higher for HEAs with high density and lower for those having a low density. As a result, a denser material may more effectively absorb γ-rays, making it useful for various industrial and medicinal applications [46]. The PE effect, which dominates the other two processes at a lower energy spectrum, is highly dependent upon the atomic number and density of the composite material. However, density has less effect above 0.1 MeV[45,48]. Unlike μ_m which has almost equal values for all HEAs in the 0.5–3 MeV range, a clear difference can be noticed in the case of μ (look at the zoomed section) that is because of the varying densities of samples. The alloys HEA8 and HEA5 exhibited maximum and minimum μ values throughout all energy regions, respectively.

The half-value layer (HVL), tenth value layer (TVL), and mean free path (λ) are the alternate methods for measuring the shielding capabilities of materials. The HVL and TVL are the thickness of material required to attenuate radiation intensity by half and 90%, respectively, and are given by the relations: $\mathrm{HVL\,(cm)} = \frac{\ln(2)}{\mu}$ and $\mathrm{TVL\,(cm)} = \frac{\ln(10)}{\mu}$ [49]. The HVL and TVL are particularly significant since they aid in calculating the amount of layer thickness required for achieving acceptable reduction [7]. Thus, HVL

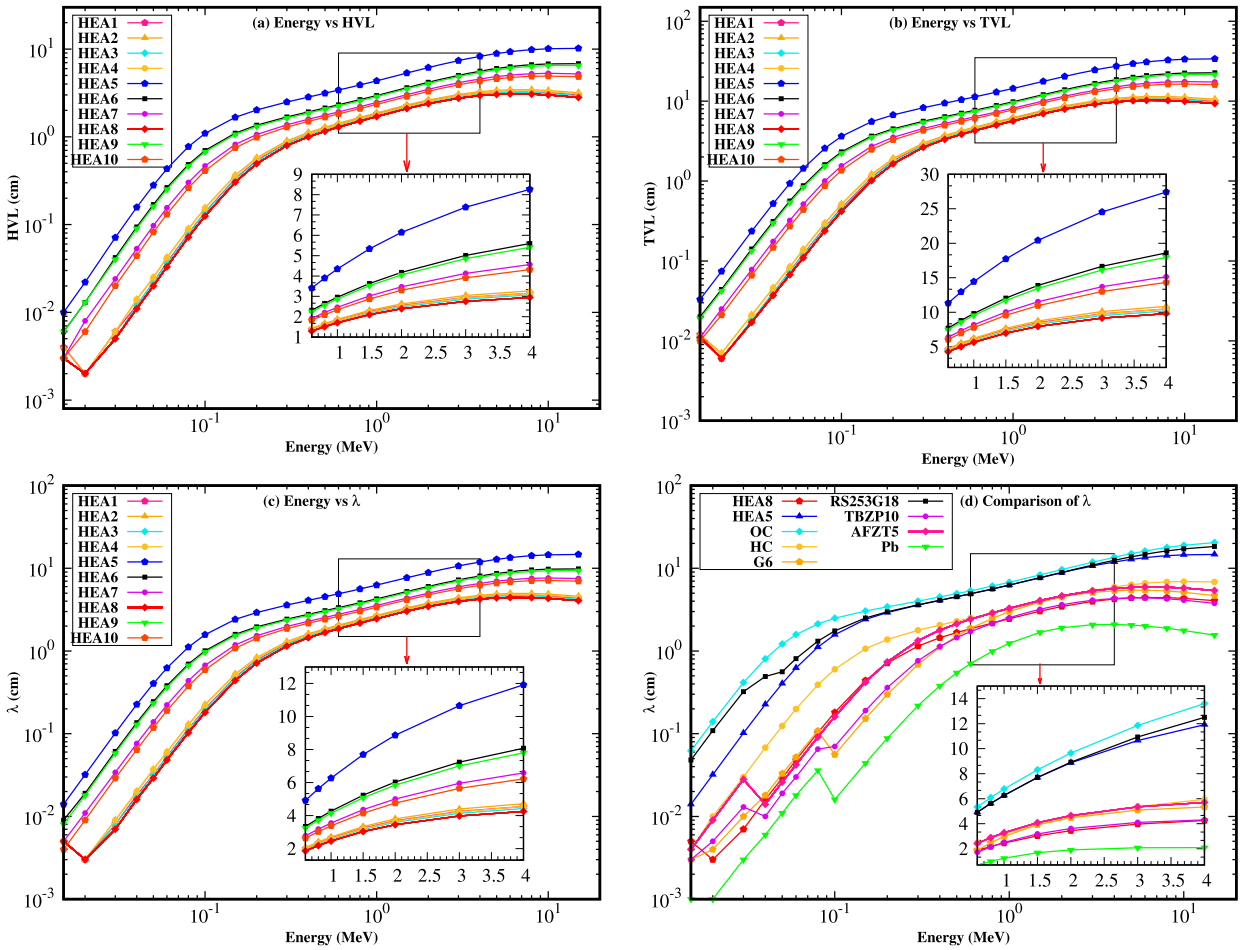

Fig. 2. Behaviors of (a) HVL, (b) TVL, (c) λ, as a function of energy of the radiation, and (d) comparison of λ with different conventional materials.

and TVL help in determining how reliable are the designed shielding materials economically. However, the mean free path (λ) is a quantity that describes how fast the radiation loses its energy by colliding with atoms of the shielding materials. It is the average distance over which a moving particle travels before changing its direction or energy because of collisions with other particles and is evaluated using: $\lambda\,(\mathrm{cm}) = \frac{1}{\mu}$ [50]. The fluctuations of HVL, TVL, and λ as a function of radiation energy are depicted in Figs. 2(a–c), respectively. As it is clear that these three parameters depend upon μ, which in turn depends on the material density, thus, these are lower for those HEAs with high density and higher for those with low density [51]. The lower the values of HVL, TVL, and λ, the better the shielding mechanism. In this sense, HEA1–HEA4 and HEA8 can act as better shields against radiation. However, HEA5 performed worst of all HEAs in terms of HVL, TVL, and λ. Further, it is observed from Figs. 2(a–c) that HVL, TVL, and λ are comparatively smaller at lower energies up to a few 100 keV but significantly higher in the upper energy region. They first increased rapidly with an increase in energy up to 0.2 MeV and then gradually up to 7 MeV due to Compton scattering, after they decreased slowly up to 15 MeV due to pair production.

As to μ_m and μ, such behavior of HVL, TVL, and λ values is explained based on the dependence of cross-section on E. By observing zoomed portions of Figs. 2(a–c), it is obvious to say that above 0.02 MeV the HVL, TVL, and λ values of selected HEAs followed the general trends as the following: HEA8 < HEA3 < HEA4 < HEA1 < HEA2 < HEA10 < HEA7 < HEA9 < HEA6 < HEA5. For 1 MeV energy, in particular, the HVL values are 1.820, 1.874, 1.772, 1.802, 4.346, 2.957, 2.461, 1.703, 2.871, and 2.342 cm, respectively, for HEA1 to HEA10. Similarly, at the same energy, TVL values are: 6.046, 6.226, 5.887, 5.988, 14.439, 9.823, 8.175, 5.656, 9.538, and 7.780 cm and the λ values are: 2.626, 2.704, 2.557, 2.600, 6.271, 4.266, 3.550, 2.456, 4.142, and 3.379 cm, respectively. Thus, HEA8 is the best, and HEA5 is the worst shield in terms of HVL, TVL, and λ.

It is feasible to compare the radiation shielding capabilities of proposed HEAs with those of conventional materials, which are often utilized in radiological protection operations. In this work, this task has been achieved in terms of λ parameters. The λ values of HEA8 (best among 10) and HEA5 (worst among 10) have been compared in Fig. 2(d) with many types of conventional shielding materials including ordinary concrete (OC) (taken from Bashter [52]), heavy concrete (HC) (taken from Olarinoye et al. [7]), bismuth borate glass systems (G6 and RS253G18) (taken from Kaur et al. [53]), Pb-based glass (TBZP10) (taken from Al-Buriahi et al. [54]), Pb-free glass (AFZT5) (taken from Sayyed et al. [55]) and pure Pb, which clearly illustrates the relationship between the HEA8 and

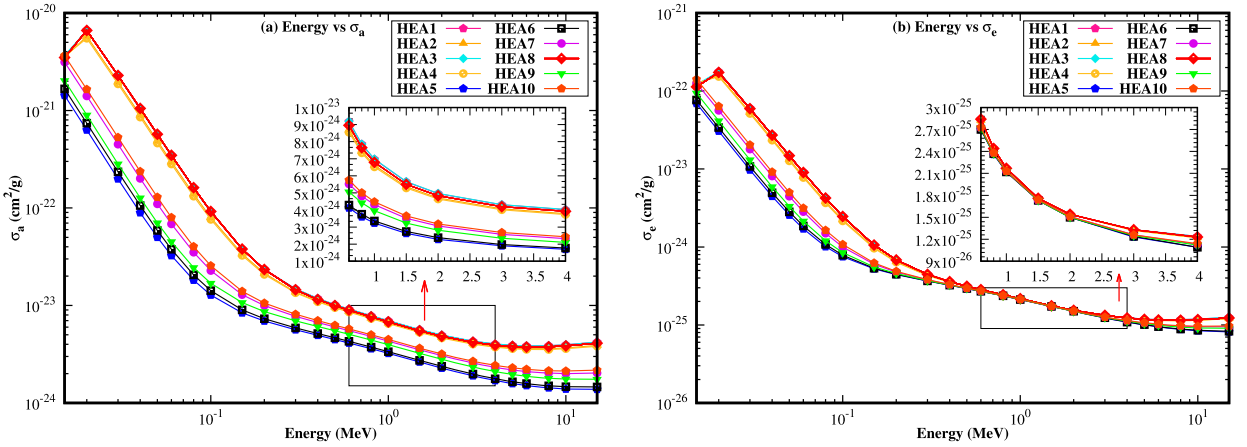

Fig. 3. Behaviors of (a) σ_a, and (b) σ_e as a function of energy of the radiation.

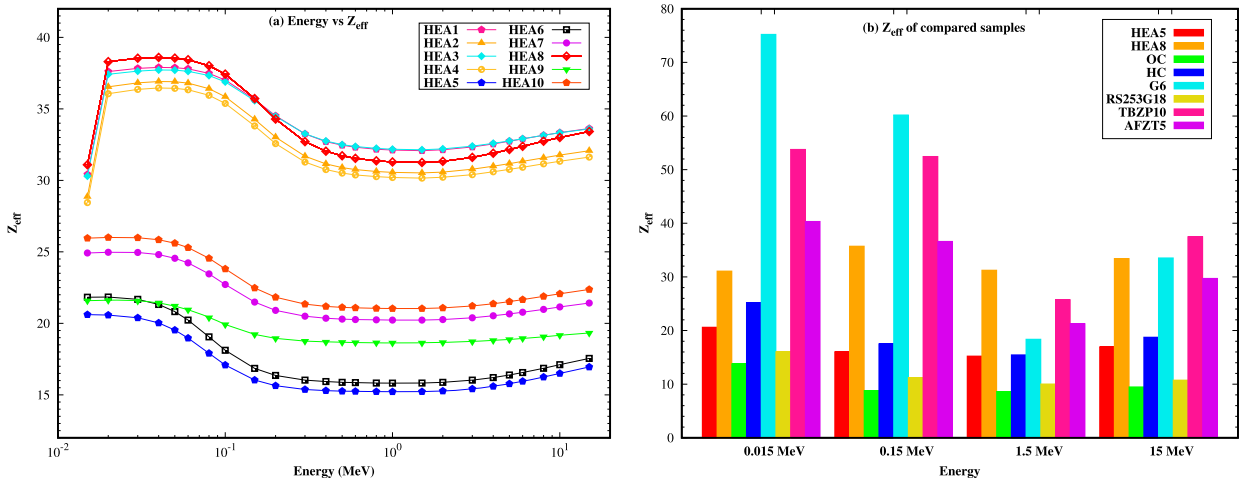

Fig. 4. (a) Behaviors of Z_{eff} as a function of energy of the radiation, and (b) comparison of Z_{eff} values of HEA5 and HEA8 with various shielding materials at different photon energies.

the other samples in terms of their λ values. Notably, for energies above 1 MeV, the HEA8 exhibits lower λ values compared to the rest of the considered samples except that of Pb. However, below this threshold, the HEA8 demonstrates higher λ values than the G5 and TBZP10 glass systems, though still lower than the remaining samples. This significant disparity highlights the exceptional shielding capabilities of HEA8 against unwanted radiation, surpassing both conventional concretes and various glass systems. Conversely, the HEA5 alloy proves to be the least effective among the samples, although it remains a superior attenuator compared to ordinary concrete and RS253G18 borate glass.

The total cross-section areas that an atom and an electron of a material offer for the interaction with radiation photons are known as atomic cross-section (σ_a) and electronic cross-section (σ_e), respectively. The σ_a is evaluated using: $\sigma_a\,(\mathrm{cm}^2/\mathrm{g}) = (\mu_m)\,\frac{\sum_i n_i A_i}{N\sum_i n_i}$, whereas σ_e, is evaluated using: $\sigma_e\,(\mathrm{cm}^2/\mathrm{g}) = \frac{\sum_i f_i A_i (\mu_m) i/Z_i}{N}$, where N is the Avogadro number, and n_i, A_i, f_i, and Z_i indicate the number of atoms, mass number, fractional abundance, and the atomic number of i^{th} component of a compound material, respectively [6]. The σ_a and σ_e give the precise probability of radiation interactions per atom or electron in each unit volume of shielding material [56]. Higher values of σ_a and σ_e result in better shielding due to the increased probability of collision between photons and atoms, resulting from the higher cross-sections. Figs. 3(a,b) exhibit their variation with energy. It can be observed from these figures that σ_a and σ_e both follow a similar trend with energy, both decreasing with the rise in energy. One noticeable difference between the two is observed from the zoomed section of the figure in the 0.5–4 MeV region, where σ_e is almost the same for all HEAs whereas σ_a is varying within samples. Both are higher for HEA1–HEA4 and HEA8 but lowest for HEA5 in overall energy values.

The effective atomic number (Z_{eff}) is the actual amount of positive (nuclear) charge experienced by an electron in a multi-electron atom, which is obtained by using the relation: $Z_{eff} = \sigma_a \sigma_e^{-1}$, where σ_a and σ_e are atomic and electronic cross-sections, respectively, discussed above [46]. High Z_{eff} values are preferred because there will be a higher chance of photon collision with substances with high Z_{eff} [6]. The high Z_{eff} for a composite material is attained if we increase the percentage composition of elements with the

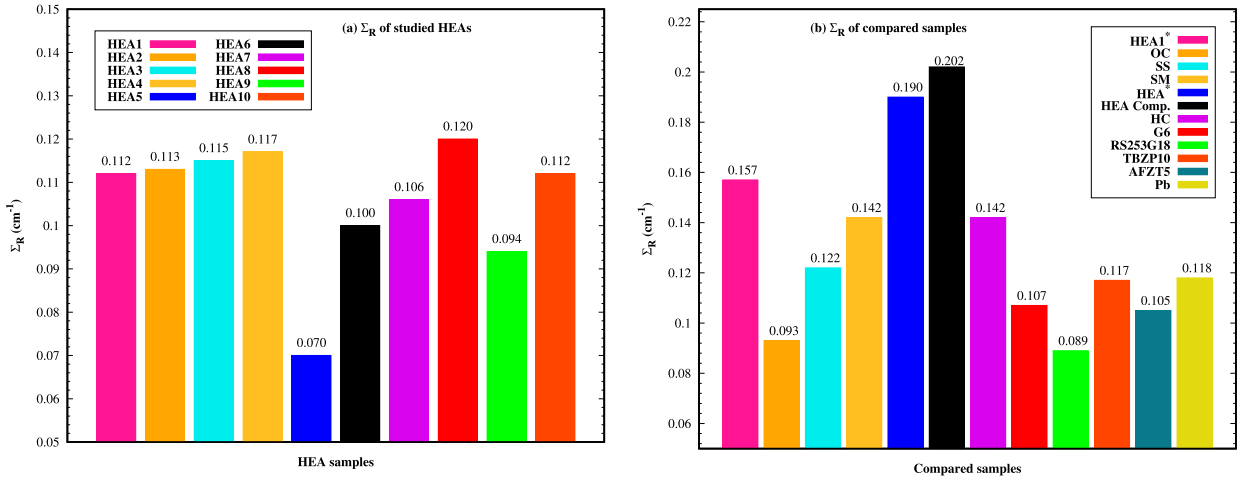

Fig. 5. (a) Σ_R of 10 different HEAs. (b) Comparison of Σ_R values with various shielding materials existing in the literature.

highest atomic number. The changing behavior of Z_{eff} with the energy of the photon is exhibited in Fig. 4(a). By inspecting the data it was found that the Z_{eff} of each HEA lies between the atomic number of the largest and smallest elements that constitute the alloy. It was also found that within the given energy range, Z_{eff} attained maximum values of 37.90, 36.91, 37.72, and 36.46 at 40 keV for HEA1–HEA4, respectively. Similarly, maximum Z_{eff} values of other HEAs were 20.61 for HEA5 at 15 keV, 21.84 and 24.97 for HEA6 and HEA7 at 20 keV, 38.60 for HEA8 at 40 keV, 21.62 and 26.01 for HEA9 and HEA10 at 20 keV, respectively. These peak values are because of different X-ray absorption edges of constituent elements, as discussed above. Generally, HEA1, HEA3, and HEA8 have higher Z_{eff} values compared with other alloys in the overall energy region. Like other parameters, the Z_{eff} varies with energy differently on various photon-matter interactions dominant regions. In contrast to the Compton and pair production interaction indices, which are directly related to Z_{eff} and its square, respectively, the photoelectric effect interaction index depends on the 5th power of Z_{eff} [7]. Thus, Z_{eff} values sharply declined in the PE process dominant region, remained almost constant in the CS dominant region, and increased slightly in the PP process dominant region. Comparing the Z_{eff} of HEA5 and HEA8 with various shielding materials at energy levels of 0.015, 0.15, 1.5, and 15 MeV (Fig. 4(b)), HEA8 exhibited higher values than OC, HC, RS253G18, and AFZT5. However, it showed slightly lower values compared to G6 and TBZP10. Conversely, HEA5 displayed higher Z_{eff} values than OC and HC, but lower values compared to the remaining materials at all four energy levels.

The fast neutron shielding capability of HEAs is the probability that a fast neutron undergoes a first collision, which removes it from the group of penetrating, uncollided neutrons. It is a parameter required to measure the neutron absorbing capacity of any material and is given by: removal cross-section $(\Sigma_R, \text{cm}^{-1}) = \sum_i \rho_i \left(\Sigma_R/\rho\right)_i$, where ρ_i and $\left(\frac{\Sigma_R}{\rho}\right)_i$ are the partial density and mass removal cross-section for the constituent element, respectively [43,46]. The assessment of Σ_R is particularly important when using the material for shielding the nuclear reactors where nuclear fission reaction occurs in the presence of neutrons. The Σ_R of HEA1–HEA10, as seen in Fig. 5(a) are 0.112, 0.113, 0.115, 0.117, 0.070, 0.100, 0.106, 0.120, 0.094, and 0.112 cm^{-1}, respectively. Thus, HEA8 exhibits the highest Σ_R value among all the investigated HEAs, as well as other materials including OC, G6, RS253G18, TBZP10, AFZT5, and Pb, positioning it as a promising neutron shielding material. This is because of its highest density of 6.93 g/cm^3. The Σ_R value depends not only on the density but also on the Z_{eff} of the composite material [7]. However, it should be noted that this value is lower than those observed for SS, SM, HEA*, HEA Comp, and HC (Fig. 5(b)). Other good shields for fast neutrons among investigated samples include the alloys HEA2, HEA3, and HEA4. The samples HEA1 and HEA10 are equally effective against fast neutrons with an equal Σ_R value of 0.112 cm^{-1}. But HEA5 with the smallest Σ_R value of 0.070 cm^{-1}, is the least effective in neutron as a neutron absorber.

In addition to all γ-ray and fast neutron shielding parameters discussed above, the build-up factors (BUFs) (i.e., exposure and energy absorption build-up factors: EBF and EABF, respectively) are other two very important parameters in radiation shielding assessments for broad beam geometry. The build-up factor is the ratio of radiation intensity scattered at a certain site to the intensity that is not interrupted there [6]. The detailed theory for the evaluation of such parameters was formulated rigorously by Harima [57]. The first step for calculating EBF and EABF is the determination of the equivalent atomic number (Z_{eq}) of composite material, which is obtained by taking the ratio of Compton to the total mass absorption coefficient of each component element and using the logarithmic interpolation approach. The standard database known as ANSI/ANS-6.4.3 reference library contains the equivalent atomic numbers and geometric-progression (G-P) fitting parameters of elements with $Z = 4$ to $Z = 40$. Thus, using these values, the logarithmic interpolation approach is applied to determine the Z_{eq} of studied HEAs. In the second step, five different G-P fitting parameters (i.e., a, b, c, d, and X_k) of each studied HEAs are determined using similar interpolation as for Z_{eq}. Finally, using these fitting parameters, the EBF and EABF values are determined for different energy (0.015 MeV $\leq$ E $\leq$ 15 MeV) and penetration depths ($0.5 \leq X \leq 40$ mfp). Thus, obtained EBF and EABF were plotted as a function of energy at seven different penetration depths: 0.5 mfp, 5 mfp, 10 mfp, 15 mfp, 20 mfp, 30 mfp, and 40 mfp. The changing behaviors of EBF and EABF of selected alloys with energy and penetration depth are depicted in Figs. 6(a–d), while rest of the figures and related data can be found in the supplementary material.

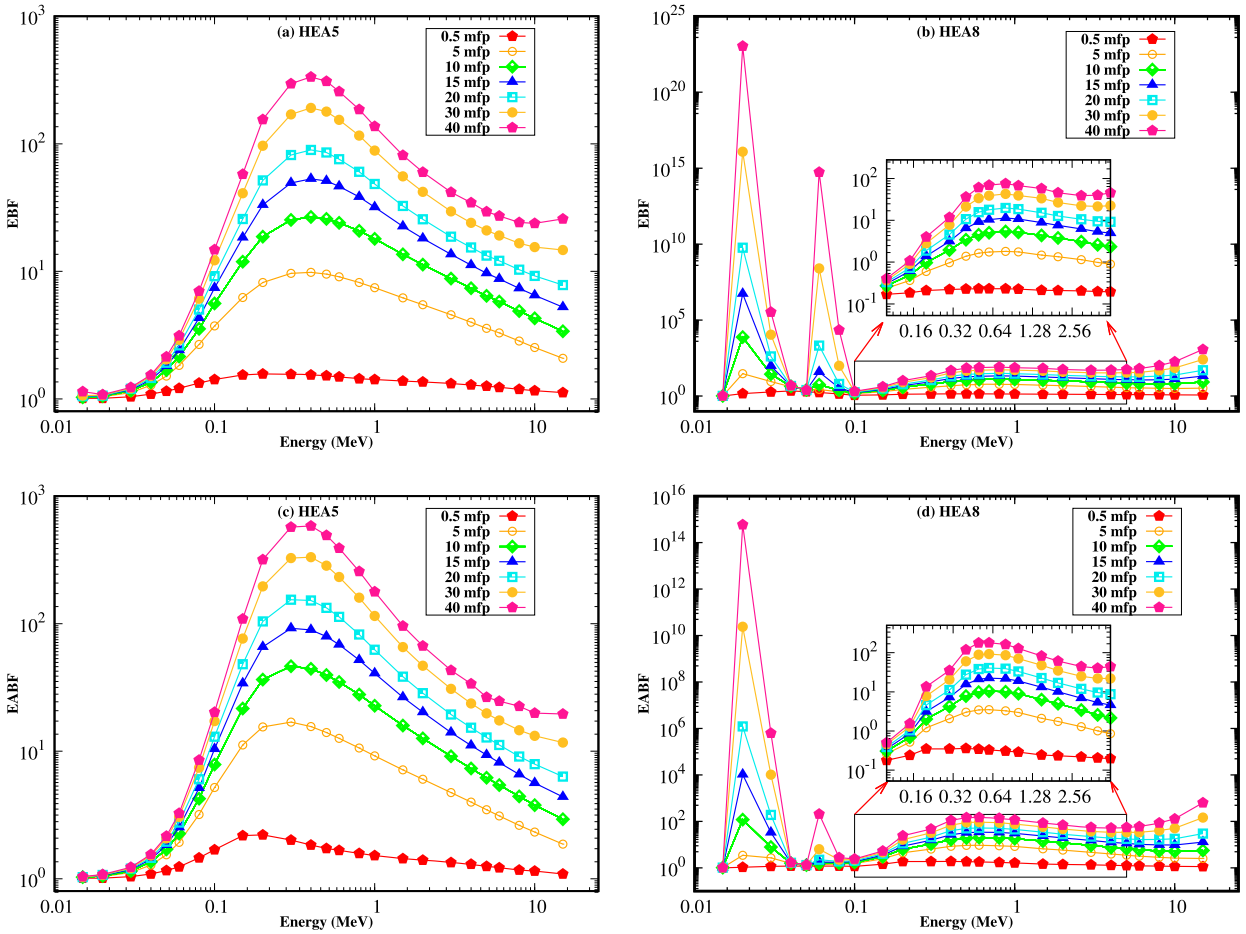

Fig. 6. Behaviors of (a-b) EBF, and (c-d) EABF of alloys HEA5 and HEA8, respectively, as a function of energy of the radiation at various penetration depths.

The natures of EBF and EABF can be described under three categories: variation with photon energy (E), penetration depths, and chemical composition of the alloys under study. It can be viewed from Figs. 6(a–d) that EBF and EABF values are very small at the smallest energies but increase to a higher value as E increases, then reduce as the energy is increased further. Unlike the PE and PP processes, which completely absorb photons in lower and higher energies, the highest BUFs in the intermediate region is the cause of Compton scattering (CS) as it reduces the energy of the incoming photon, thereby failing to remove it [45]. Such interactions boost the production of additional photons, which increase the incidence of contact inside the substance, thereby increasing EBF and EABFs [56]. Some abrupt increase in build-up factors at 20 keV is the cause of the K X-ray absorption edge of Mo (19.99 keV) because the Compton scattering cross-section varies as Z^{4-5} for atoms having high atomic numbers. Additionally, the EABF values are higher than the EBF for most photon energies for all HEAs. This means that due to the larger Z_{eq} of HEAs, higher energy is absorbed in the air than in the media [46].

Figs. 7(a–d) describe how EBF and EABF change with E at particular depths: 5 mfp and 40 mfp. Further, it is clear from Figs. 6(a–d) that the EBF and EABF exhibit a directly proportional relationship with the penetration depth. Figs. 8(a, b) show the variation of EBF and EABF with penetration depth at 0.6 MeV particular energy. The increase in EBF and EABF with penetration depths can be clarified based on the fact that scattering centers grow as the penetration depth rises, increasing the scattered photon multiplication coefficient and, thus, the likelihood of Compton scattering [58]. Also, it is observed from Figs. 7(a–d) and Figs. 8(a, b) that EBF and EABF vary with the chemical composition (i.e., with Z_{eff}). We found by deep inspection of the data and figures that the alloys HEA8 and HEA5 have the lowest and highest EBF and EABF values in the intermediate (0.1–5 MeV) energy range, respectively. Thus, HEA8 will be the best shielding agent, while HEA5 will be the worst in this range. The lowest EBF and EABF values in this range provided by HEA8 were 1.13 and 1.17, respectively. Alloys HEA1, HEA2, HEA3, and HEA4 also have comparable EBF and EABF values in this range. However, in the lower (0.015–0.08 MeV) and higher (5–15 MeV) energy regions, HEA10 has the lowest EBF and EABF values. The alloys HEA5, HEA6, and HEA9 also have smaller EBF and EABF in these regions hence they will also be better shields against the γ-rays. As HEA8 has the highest EBF and EABF values in low and high-energy regions, it is thus not preferable to use it as a shielding material in these regions.

Finally, it is also a necessary task to assess the damage that H^1 and He^{+2} ions pose to the target HEA samples as well as their durability against such radiations [6]. This task has been carried out in terms of two different parameters namely, total stopping

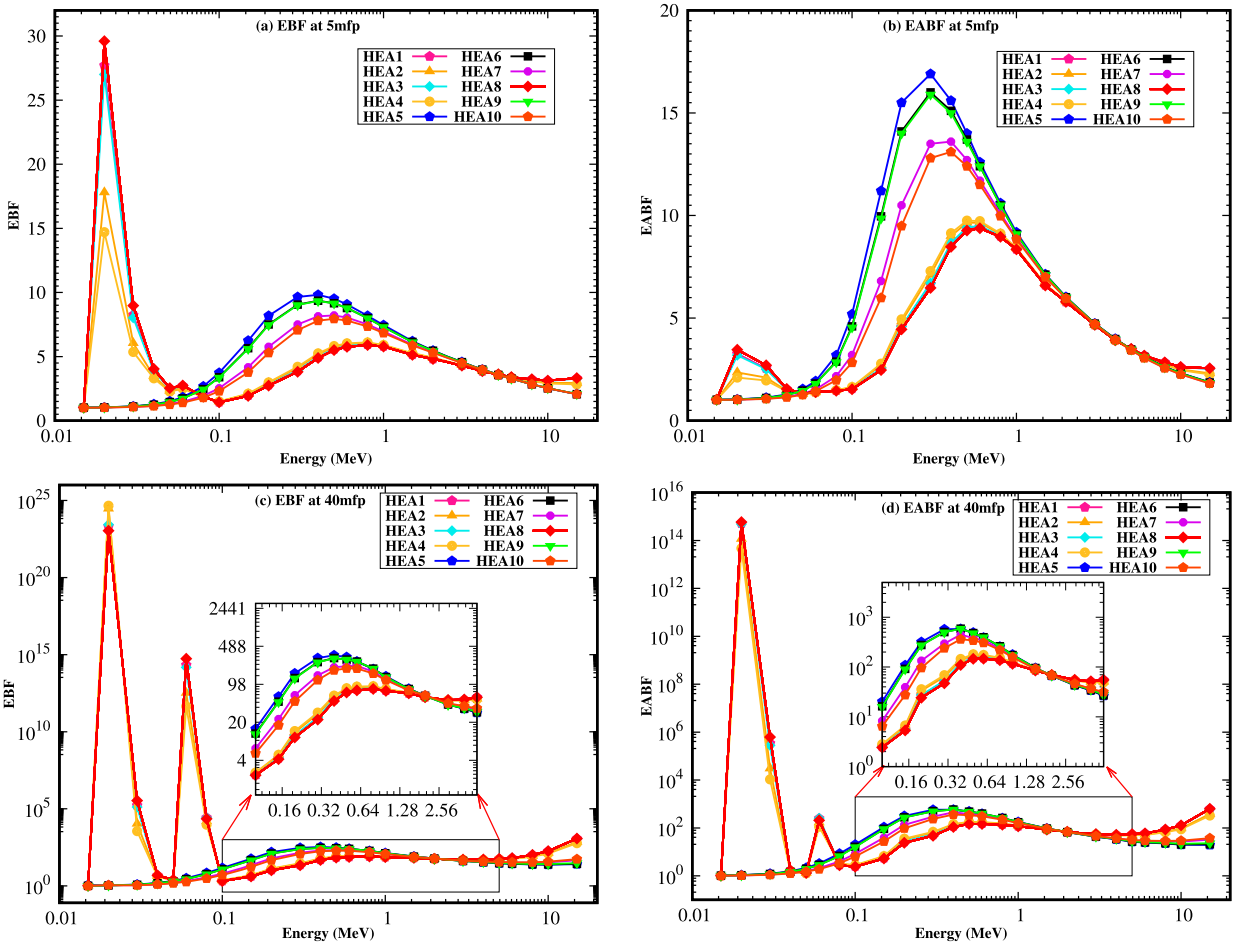

Fig. 7. Behaviors of EBF and EABF as a function of energy of the radiation at (a-b) 5 mfp and (c-d) 40 mfp penetration depth.

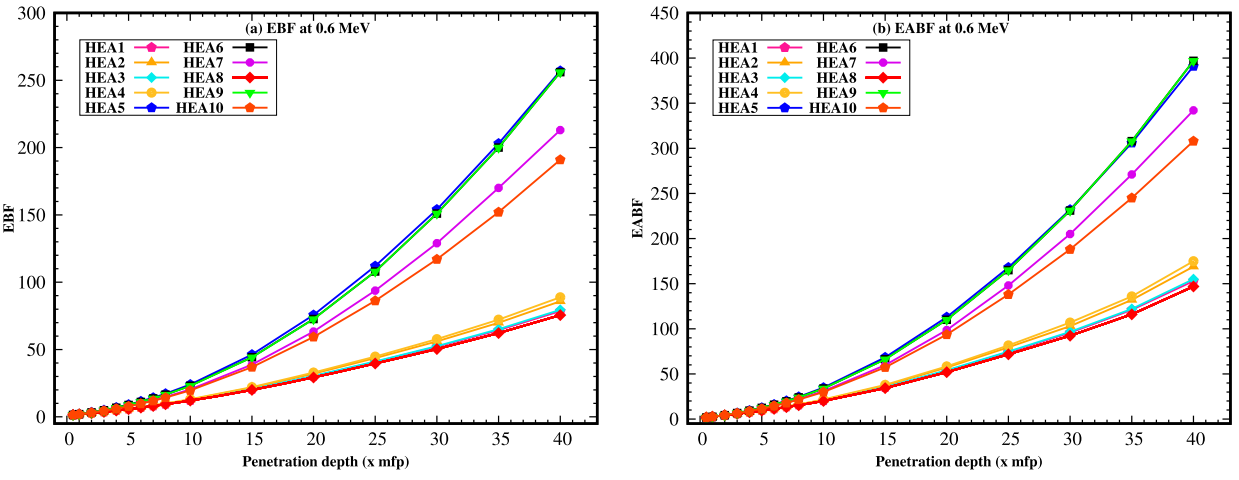

Fig. 8. Behaviors of (a) EBF and (b) EABF as a function of penetration depth at 0.6 MeV.

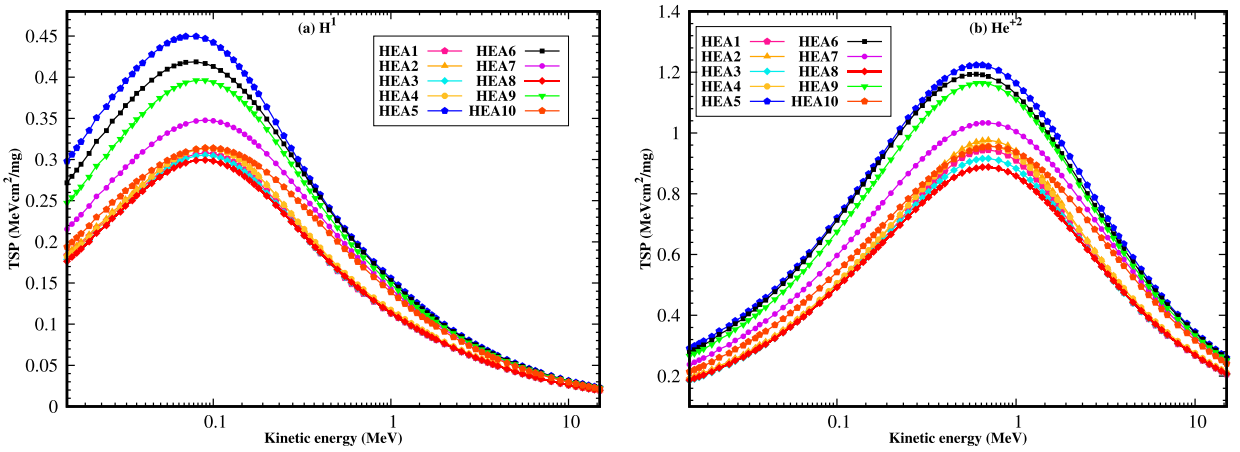

Fig. 9. Behaviors of TSP against (a) H^1 (proton) and (b) He^{+2} (alpha particle) ions as a function of their kinetic energy.

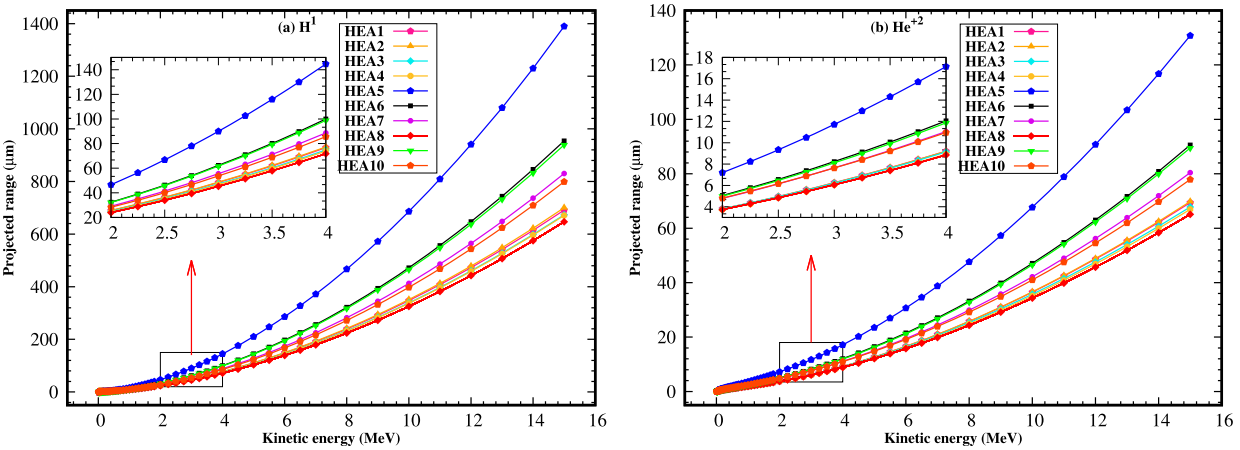

Fig. 10. Behaviors of PR against (a) H^1 (proton) and (b) He^{+2} (alpha particle) ions as a function of their kinetic energy.

power (TSP, MeV cm^2/mg) and projected range (PR, μm) by using the SRIM Monte Carlo program [44]. The TSP is the sum of electronic stopping and nuclear-stopping powers, which are the results of interactions of ions with atomic electrons and the atomic nucleus, respectively [6]. It is the rate of loss of kinetic energy of ion per unit distance per unit density of the HEA samples that it traverses through and is calculated using the Bethe-Bloch formula. The PR, which may on the other side be defined as the mean path length that an ion traverses through the samples before coming to the rest, should be minimum for the best protection against such ions [3,51]. The TSP and PR are the two crucial variables to consider when evaluating a material's ability to block radiation [59]. The behaviors of TSP and PR as the function of the kinetic energy of H^1 and He^{+2} ions in 0.015–15 MeV region against HEA samples are depicted in Figs. 9(a, b) and Figs. 10(a, b), respectively. It can be seen from Figs. 9(a, b) that the TSP of both ions depends a great deal on their kinetic energy, increasing initially up to attaining maximum values and then decreasing again to a minimum. Moreover, TSP for H^1 ions is seen to rise to a maximum value (at about 0.09 MeV) faster than He^{+2} ions (that attained maximum at about 0.7 MeV), which is due the lighter mass of H^1 ions than the He^{+2} ions. The energy loss from the collision happens more quickly in the orbit because the H^1 ion is lighter than the He^{+2} ion [6]. Among 10 investigated alloys, HEA8 and HEA5 have the lowest and the highest TSP values, respectively, for both H^1 and He^{+2} at all ions energy. For example, the TSP of investigated HEAs against H^1 ions at 0.09 MeV are 0.3075, 0.3137, 0.3053, 0.3140, 0.4468, 0.4167, 0.3477, 0.2994, 0.3962, 0.3139 MeVcm^2/mg, for HEA1 to HEA10, respectively. Similarly, the TSP values are 0.9439, 0.9760, 0.9157, 0.9584, 1.2190, 1.1860, 1.0330, 0.8879, 1.1620, 0.9548 MeV cm^2/mg at 0.7 MeV kinetic energy of He^{+2} ions. Meanwhile, the variations in PR values of investigated HEAs as the function of the kinetic energy of ions have been illustrated in Figs. 10(a, b). As seen from the graphics, PR increases with the rise in ion energy. This is obvious because of the reason that highly energetic ion penetrates deeper into the material. At a given particular energy, the PR value of H^1 is very high compared to that of He^{+2} ion, which could be the cause of its less collision probability with the target atoms due to its smaller size. Similar to TSP, the HEA5 and HEA8 samples have the largest and the smallest PR values among all HEA samples, respectively. Thus, it can be concluded from the SRIM calculations that HEA8 is the most effective alloy in shielding not only the γ-rays but the H^1/He^{+2} ions as well. By contrast, HEA5 is the least effective one against such ions.

4. Conclusions

In the present study, we investigated the radiation protection efficiencies of recently developed 10 different low-density HEAs using the user-friendly online server: Phy-X/PSD. The software facilitated us with the various important parameters such as μ_m, μ, HVL, TVL, λ, σ_a, σ_e, and Z_{eff} in the wide energy range (i.e., 15 keV–15 MeV). A comparative analysis was conducted between the attenuation results obtained for HEAs and various types of shielding materials reported in the existing literature. The fast neutron shielding capacity of alloys was also determined in terms of Σ_R. The build-up factors (EBF and EABF) were calculated in 0.015–15 MeV by the GP-fitting interpolation method for which fitting parameters were obtained from the standard ANSI database. Finally, the stopping powers of HEAs against H^1/He^{+2} ions were evaluated using the SRIM Monte Carlo program in terms of MSP and PR. Based on the results discussed above, the following conclusions are made.

1. The alloy sample HEA8 ($Al_{3.88}Cr_{14.95}Mo_{27.58}Nb_{26.71}Ti_{13.76}Zr_{13.11}$) has the highest μ and μ_m with the lowest HVL, TVL and λ values.
2. The two different cross-sections: σ_a and σ_e, and hence Z_{eff} are highest for HEA8 and lowest for HEA5 alloy in the given energy range.
3. The alloy sample HEA8 also has the best fast neutron shielding capability with the highest value of Σ_R whereas HEA5 ($Al_{16.57}Li_{4.26}Mg_{7.46}Sc_{27.61}Ti_{44.09}$) has the lowest Σ_R value.
4. SRIM Monte Carlo calculations revealed the lowest MSP and PR values for HEA8 and the highest ones for HEA5 indicating the superiority of HEA8 alloy in shielding H^1/He^{+2} ions.
5. Many variations in shielding characteristics were noticed in lower energy regions due to different X-ray absorption edges of constituent elements.
6. Lowest build-up factors (EBF and EABF) were also observed for HEA8 in intermediate (0.1–5 MeV) energy region and HEA10 ($Mg_{10.77}Al_{11.96}Mn_{24.35}Fe_{24.75}Cu_{28.17}$) in lower (0.015–0.08 MeV) and higher (5–15 MeV) energy regions.

Finally, it can be concluded that HEAs might be better alternatives to traditional lead-based compounds as radiation, fast neutron, and charged particles shielding materials and hence apply to a range of shielding fields. Nevertheless, further experimental validation might be necessary to ascertain their viability for practical applications.

CRediT authorship contribution statement

Basanta Subedi: Performed the experiments; Analyzed and interpreted the data; Wrote the paper.
Jeevan Paudel: Contributed reagents, materials, analysis tools or data.
Tika Ram Lamichhane: Conceived and designed the experiments; Wrote the paper.

Declaration of competing interest

The authors declare that they have no known competing financial interests or personal relationships that could have appeared to influence the work reported in this paper.

Data availability

Data will be made available on request.

Appendix A. Supplementary material

Supplementary material related to this article can be found online at https://doi.org/10.1016/j.heliyon.2023.e17725.

References

[1] B. Oto, N. Yıldız, T. Korkut, E. Kavaz, Neutron shielding qualities and gamma ray buildup factors of concretes containing limonite ore, Nucl. Eng. Des. 293 (2015) 166–175.
[2] H. Gökçe, O. Güngör, H. Yılmaz, An online software to simulate the shielding properties of materials for neutrons and photons: Ngcal, Radiat. Phys. Chem. 185 (2021) 109519.
[3] W. Chaiphaksa, S. Yonphan, N. Chanthima, J. Kaewkhao, N. Sanwaranatee, Computational approach of alpha and proton interaction of gadolinium bismuth borate glass system using SRIM program, Mater. Today Proc. 65 (2022) 2416–2420.
[4] M. Sayyed, K.M. Kaky, D. Gaikwad, O. Agar, U. Gawai, S. Baki, Physical, structural, optical and gamma radiation shielding properties of borate glasses containing heavy metals (Bi2O3/MoO3), J. Non-Cryst. Solids 507 (2019) 30–37.
[5] A. Mostafa, S.A. Issa, M. Sayyed, Gamma ray shielding properties of PbO-B2O3-P2O5 doped with WO3, J. Alloys Compd. 708 (2017) 294–300.
[6] M. Kamislioglu, An investigation into gamma radiation shielding parameters of the (Al: Si) and (Al+Na): Si-doped international simple glasses (ISG) used in nuclear waste management, deploying Phy-X/PSD and SRIM software, J. Mater. Sci., Mater. Electron. 32 (9) (2021) 12690–12704.
[7] O. Olarinoye, C. Oche, Gamma-ray and fast neutron shielding parameters of two new titanium-based bulk metallic glasses, Iran. J. Med. Phys. 18 (2) (2021) 139–147.
[8] M. Al-Buriahi, Z. Alrowaili, C. Eke, J.S. Alzahrani, I. Olarinoye, C. Sriwunkum, Optical and radiation shielding studies on tellurite glass system containing ZnO and Na2O, Optik 257 (2022) 168821.

[9] B. Alım, E. Şakar, A. Baltakesmez, İ. Han, M. Sayyed, L. Demir, Experimental investigation of radiation shielding performances of some important AISI-coded stainless steels: Part I, Radiat. Phys. Chem. 166 (2020) 108455.
[10] S. Yin, H. Wang, S. Wang, J. Zhang, Y. Zhu, Effect of B2O3 on the radiation shielding performance of telluride lead glass system, Crystals 12 (2) (2022) 178.
[11] X. Zhang, Y. Li, C. Li, F. Yang, Z. Jiang, L. Xue, Z. Shao, Z. Zhao, M. Xie, S. Yu, A novel (La0.2Ce0.2Gd0.2Er0.2Tm0.2)2(WO4) 3 high-entropy ceramic material for thermal neutron and gamma-ray shielding, Mater. Des. 205 (2021) 109722.
[12] B. Oto, E. Kavaz, H. Durak, A. Aras, Z. Madak, Effect of addition of molybdenum on photon and fast neutron radiation shielding properties in ceramics, Ceram. Int. 45 (17) (2019) 23681–23689.
[13] M. Sayyed, E. Hannachi, Y. Slimani, M.U. Khandaker, M. Elsafi, Radiation shielding properties of bi-ferroic ceramics added with cnts, Radiat. Phys. Chem. 200 (2022) 110096.
[14] Y. Slimani, M.K. Hamad, I. Olarinoye, Y. Alajerami, M. Sayyed, M. Almessiere, M. Mhareb, Determination of structural features of different perovskite ceramics and investigation of ionizing radiation shielding properties, J. Mater. Sci., Mater. Electron. 32 (2021) 20867–20881.
[15] M. Mhareb, Y. Slimani, Y. Alajerami, M. Sayyed, E. Lacomme, M. Almessiere, Structural and radiation shielding properties of BaTiO3 ceramic with different concentrations of bismuth and ytterbium, Ceram. Int. 46 (18) (2020) 28877–28886.
[16] K. Srinivasan, E.J.J. Samuel, Evaluation of radiation shielding properties of the polyvinyl alcohol/iron oxide polymer composite, J. Med. Phys. 42 (4) (2017) 273.
[17] B. Körpınar, B.C. Öztürk, N.F. Çam, H. Akat, Investigations on thermal and radiation shielding properties of the poly (hydroxyethyl methacrylate-co-styrene)/tungsten (vi) oxide composites, Prog. Nucl. Energy 126 (2020) 103424.
[18] T. Bel, C. Arslan, N. Baydogan, Radiation shielding properties of poly (methyl methacrylate)/colemanite composite for the use in mixed irradiation fields of neutrons and gamma rays, Mater. Chem. Phys. 221 (2019) 58–67.
[19] M. Sayyed, B. Albarzan, A.H. Almuqrin, A.M. El-Khatib, A. Kumar, D.I. Tishkevich, A.V. Trukhanov, M. Elsafi, Experimental and theoretical study of radiation shielding features of CaO-K2O-Na2O-P2O5 glass systems, Materials 14 (14) (2021) 3772.
[20] D.Ş. Baykal, H.O. Tekin, R.B.Ç. Mutlu, An investigation on radiation shielding properties of borosilicate glass systems, Int. J. Comput. Exp. Sci. Eng. 7 (2) (2021) 99–108.
[21] I. Akkurt, R.B. Malidarre, T. Kavas, Monte Carlo simulation of radiation shielding properties of the glass system containing Bi2O3, Eur. Phys. J. Plus 136 (3) (2021) 1–10.
[22] H. Yaykaşlı, H. Eskalen, Y. Kavun, M. Gögebakan, Microstructural, thermal, and radiation shielding properties of Al50B25Mg25 alloy prepared by mechanical alloying, J. Mater. Sci., Mater. Electron. 33 (5) (2022) 2350–2359.
[23] J.S. Alzahrani, Z. Alrowaili, C. Eke, Z.M. Mahmoud, C. Mutuwong, M. Al-Buriahi, Nuclear shielding properties of Ni-, Fe-, Pb-, and W-based alloys, Radiat. Phys. Chem. 195 (2022) 110090.
[24] M.F. Turhan, F. Akman, A. Taşer, K. Dilsiz, H. Oğul, M.R. Kaçal, O. Agar, Gamma radiation shielding performance of cuxag (1-x)-alloys: experimental, theoretical and simulation results, Prog. Nucl. Energy 143 (2022) 104036.
[25] A. Levet, E. Kavaz, Y. Özdemir, An experimental study on the investigation of nuclear radiation shielding characteristics in iron-boron alloys, J. Alloys Compd. 819 (2020) 152946.
[26] M.K. Hamad, Evaluation of photon shielding properties for new refractory tantalum-rich sulfides Ta9(XS3)2 alloys: a study with the mcnp-5, Ann. Nucl. Energy 184 (2023) 109687.
[27] B. Subedi, T.R. Lamichhane, Radiation shielding properties of low-density Ti-based bulk metallic glass composites: a computational study, Phys. Scr. 98 (3) (2023) 035003.
[28] K. Tseng, Y. Yang, C. Juan, T. Chin, C. Tsai, J. Yeh, A light-weight high-entropy alloy Al20Be20Fe10Si15Ti35, Sci. China, Technol. Sci. 61 (2) (2018) 184–188.
[29] Z. Tang, T. Yuan, C.-W. Tsai, J.-W. Yeh, C.D. Lundin, P.K. Liaw, Fatigue behavior of a wrought Al0.5CoCrCuFeNi two-phase high-entropy alloy, Acta Mater. 99 (2015) 247–258.
[30] B. Gludovatz, A. Hohenwarter, D. Catoor, E.H. Chang, E.P. George, R.O. Ritchie, A fracture-resistant high-entropy alloy for cryogenic applications, Science 345 (6201) (2014) 1153–1158.
[31] A.O. Gul, E. Kavaz, O. Basgoz, O. Guler, G. ALMisned, E. Bahceci, M.G. Albayrak, H. Tekin, Newly synthesized NiCoFeCrW high-entropy alloys (HEAs): multiple impacts of B4C additive on structural, mechanical, and nuclear shielding properties, Intermetallics 146 (2022) 107593.
[32] E. Sakar, O. Guler, B. Alım, Y. Say, B. Dikici, A comprehensive study on structural properties, photon and particle attenuation competence of CoNiFeCr-Ti/Al high entropy alloys (HEAs), J. Alloys Compd. 931 (2023) 167561.
[33] Y. Shi, B. Yang, X. Xie, J. Brechtl, K.A. Dahmen, P.K. Liaw, Corrosion of Al xCoCrFeNi high-entropy alloys: Al-content and potential scan-rate dependent pitting behavior, Corros. Sci. 119 (2017) 33–45.
[34] O. Senkov, S. Senkova, D. Miracle, C. Woodward, Mechanical properties of low-density, refractory multi-principal element alloys of the Cr–Nb–Ti–V–Zr system, Mater. Sci. Eng. A 565 (2013) 51–62.
[35] Z. Aygun, Study on radiation shielding characteristics of refractory high entropy alloys by epixs code, Acta Phys. Pol. A 143 (1) (2023).
[36] K.M. Youssef, A.J. Zaddach, C. Niu, D.L. Irving, C.C. Koch, A novel low-density, high-hardness, high-entropy alloy with close-packed single-phase nanocrystalline structures, Mater. Res. Lett. 3 (2) (2015) 95–99.
[37] R.K. Mishra, R.R. Shahi, A novel low-density semi-hard magnetic Al20Fe20Mg20Ni20Ti20 high entropy alloy, J. Magn. Magn. Mater. 516 (2020) 167342.
[38] O.A. Waseem, H.J. Ryu, Combinatorial development of the low-density high-entropy alloy Al10Cr20Mo20Nb20Ti20Zr10 having gigapascal strength at 1000 c, J. Alloys Compd. 845 (2020) 155700.
[39] P. Chauhan, S. Yebaji, V.N. Nadakuduru, T. Shanmugasundaram, Development of a novel light weight Al35Cr14Mg6Ti35V10 high entropy alloy using mechanical alloying and spark plasma sintering, J. Alloys Compd. 820 (2020) 153367.
[40] V.K. Pandey, Y. Shadangi, V. Shivam, J. Basu, K. Chattopadhyay, B. Majumdar, B. Sarma, N.K. Mukhopadhyay, Synthesis, characterization and thermal stability of nanocrystalline MgAlMnFeCu low-density high-entropy alloy, Trans. Indian Inst. Met. 74 (1) (2021) 33–44.
[41] E. Kavaz, A.O. Gul, O. Basgoz, O. Guler, G. ALMisned, E. Bahceci, S.H. Guler, H.O. Tekin, Boron nitride nanosheet-reinforced WNiCoFeCr high-entropy alloys: the role of B4C on the structural, physical, mechanical, and radiological shielding properties, Appl. Phys. A 128 (8) (2022) 1–15.
[42] K. Wang, J. Hu, T. Chen, W. Zhang, H. Fan, Y. Feng, Z. Zhao, K. Wang, Flexible low-melting point radiation shielding materials: soft elastomers with GaInSnPbBi high-entropy alloy inclusions, Macromol. Mater. Eng. 306 (12) (2021) 2100457.
[43] E. Şakar, Ö.F. Özpolat, B. Alım, M. Sayyed, M. Kurudirek, Phy-X/PSD: development of a user friendly online software for calculation of parameters relevant to radiation shielding and dosimetry, Radiat. Phys. Chem. 166 (2020) 108496.
[44] J.F. Ziegler, M.D. Ziegler, J.P. Biersack, SRIM—the stopping and range of ions in matter (2010), Nucl. Instrum. Methods Phys. Res., Sect. B, Beam Interact. Mater. Atoms 268 (11–12) (2010) 1818–1823.
[45] H.O. Tekin, G. ALMisned, G. Susoy, H.M. Zakaly, S.A. Issa, G. Kilic, Y.S. Rammah, G. Lakshminarayana, A. Ene, A detailed investigation on highly dense CuZr bulk metallic glasses for shielding purposes, Open Chem. 20 (1) (2022) 69–80.
[46] N. Sabry, M.S. Alqahtani, M. Reben, H. Algarni, A. Umar, H.B. Albargi, I. Yahia, H. Zahran, et al., Gamma-ray attenuation properties and fast neutron removal cross-section of Cu2CdSn3S8 and binary sulfide compounds (Cu/Cd/Sn S) using Phy-X/PSD software, Radiat. Phys. Chem. 193 (2022) 109989.
[47] M. Sayyed, K.M. Kaky, E. Şakar, U. Akbaba, M.M. Taki, O. Agar, Gamma radiation shielding investigations for selected germanate glasses, J. Non-Cryst. Solids 512 (2019) 33–40.

[48] Photon buildup factors for some tissues and phantom materials for penetration depths up to 100 mfp, J. Nucl. Res. Dev. 13 (2017) 57–67.
[49] H. Sahadath, A.S. Mollah, K.A. Kabir, M.F. Huq, Calculation of the different shielding properties of locally developed ilmenite-magnetite (IM) concrete, Radioprotection 50 (3) (2015) 203–207.
[50] T. Kaur, J. Sharma, T. Singh, Feasibility of Pb-Zn binary alloys as gamma rays shielding materials, Int J. Pure Appl. Phys 13 (1) (2017) 222–225.
[51] U. Perişanoğlu, Assessment of nuclear shielding and alpha/proton mass stopping power properties of various metallic glasses, Appl. Phys. A 125 (11) (2019) 1–11.
[52] I. Bashter, Calculation of radiation attenuation coefficients for shielding concretes, Ann. Nucl. Energy 24 (17) (1997) 1389–1401.
[53] P. Kaur, K. Singh, S. Thakur, P. Singh, B. Bajwa, Investigation of bismuth borate glass system modified with barium for structural and gamma-ray shielding properties, Spectrochim. Acta, Part A, Mol. Biomol. Spectrosc. 206 (2019) 367–377.
[54] M.S. Al-Buriahi, F. El-Agawany, C. Sriwunkum, H. Akyıldırım, H. Arslan, B.T. Tonguç, R. El-Mallawany, Y. Rammah, Influence of Bi2O3/PbO on nuclear shielding characteristics of lead-zinc-tellurite glasses, Physica B, Condens. Matter 581 (2020) 411946.
[55] M. Sayyed, H. Akyildirim, M. Al-Buriahi, E. Lacomme, R. Ayad, G. Bonvicini, Oxyfluoro-tellurite-zinc glasses and the nuclear-shielding ability under the substitution of AlF3 by ZnO, Appl. Phys. A 126 (2020) 1–12.
[56] Y. Aboudeif, M. Alqahtani, E. Massoud, I. Yaha, E. Yousef, An evaluation of the radiation protection characteristics of prototyped oxide glasses utilising Phy-X/PSD software, J. Instrum. 15 (08) (2020) P08005.
[57] Y. Harima, An approximation of gamma-ray buildup factors by modified geometrical progression, Nucl. Sci. Eng. 83 (2) (1983) 299–309.
[58] T. Singh, A. Kaur, J. Sharma, P.S. Singh, Gamma rays' shielding parameters for some Pb-Cu binary alloys, Int. J. Eng. Sci. Technol. 21 (5) (2018) 1078–1085.
[59] N. Al-Harbi, M. Sayyed, R. Kurtulus, M. Kamışlıoğlu, A. Kumar, A.M. Alhuthali, T. Kavas, Y. Al-Hadeethi, Understanding the role of Bi2O3 in the P2O5–CaO–Na2O–K2O glass system in terms of physical, structural and radiation shielding properties, J. Mater. Sci., Mater. Electron. 32 (2021) 11649–11665.